Journal of Advanced Research 58 (2024) 1–11

Contents lists available at ScienceDirect

Journal of Advanced Research

journal homepage: www.elsevier.com/locate/jare

Original Article

Structural assessment of OsNIP2;1 highlighted critical residues defining solute specificity and functionality of NIP class aquaporins

Yogesh Sharma [a,b], Vandana Thakral [a,c], Gaurav Raturi [a,c], Kshatresh Dutta Dubey [d], Humira Sonah [a,g], Ashwani Pareek [a], Tilak Raj Sharma [a,e], Rupesh Deshmukh [a,f,g,*]

[a] National Agri-Food Biotechnology Institute, Mohali, Punjab, India
[b] Regional Centre for Biotechnology, Faridabad, Haryana (NCR Delhi), India
[c] Department of Biotechnology, Panjab University, Chandigarh, India
[d] Department of Chemistry, School of Natural Sciences, Shiv Nadar Institute of Eminence, Gautam Buddha Nagar, Uttar Pradesh, India
[e] Indian Council of Agricultural Research, Division of Crop Science, Krishi Bhavan, New Delhi, India
[f] Plaksha University, Mohali, Punjab, India
[g] Department of Biotechnology, Central University of Haryana, Mahendragarh, Haryana, India

HIGHLIGHTS

- The free energy landscape for silicon and arsenic permeation was traced.
- The transport cycle reveals novel energy constraints on silicon and arsenic permeation.
- Predicted functionally important residues were validated in yeast.
- Altering conserved amino acids in loop C and loop D directly influenced metalloid uptake of OsNIP2;1.
- Protein variants with lower arsenic uptake were identified to reduce arsenic levels with minimum counterproductive effects.

GRAPHICAL ABSTRACT

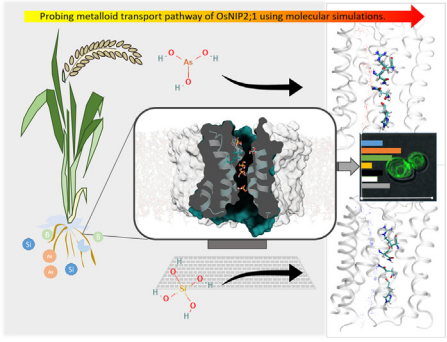

ARTICLE INFO

Article history:
Received 20 October 2022
Revised 30 April 2023
Accepted 30 April 2023
Available online 8 May 2023

Keywords:
Orthosilicic acid
Arsenous acid
Solute specificity
Molecular dynamics
plant aquaporins
Metalloid
Silicon
Arsenic

ABSTRACT

Introduction: Nodulin-26-like intrinsic proteins (NIPs) are integral membrane proteins belonging to the aquaporin family, that facilitate the transport of neutral solutes across the bilayer. The OsNIP2;1 a member of NIP-III class of aquaporins is permeable to beneficial elements like silicon and hazardous arsenic. However, the atomistic cross-talk of these molecules traversing the OsNIP2;1 channel is not well understood.

Objective: Due to the lack of genomic variation but the availability of high confidence crystal structure, this study aims to highlight structural determinants of metalloid permeation through OsNIP2;1.

Methods: The molecular simulations, combined with site-directed mutagenesis were used to probe the role of specific residues in the metalloid transport activity of OsNIP2;1.

Results: We drew energetic landscape of OsNIP2;1, for silicic and arsenous acid transport. Potential Mean Force (PMF) construction illuminate three prominent energetic barriers for metalloid passage through the pore. One corresponds to the extracellular molecular entry in the channel, the second located on ar/R filter, and the third size constriction in the cytoplasmic half. Comparative PMF for silicic acid and arsenous acid elucidate a higher barrier for silicic acid at the cytoplasmic constrict resulting in longer residence time for silicon. Furthermore, our simulation studies explained the importance of conserved residues in loop-C and loop-D with a direct effect on pore dynamics and metalloid transport. Next we assessed

* Corresponding author at: Department of Biotechnology, Central Universityof Haryana, Mahendragarh, Haryana 123031, India.
E-mail address: rupesh.deshmukh@cuh.ac.in (R. Deshmukh).

https://doi.org/10.1016/j.jare.2023.04.020

contribution of predicted key residues for arsenic uptake, by functional complementation in yeast. With the aim of reducing arsenic uptake while maintaining beneficial elements uptake, we identified novel OsNIP2;1 mutants with substantial reduction in arsenic uptake in yeast.

Conclusion: We provide a comprehensive assessment of pore lining residues of OsNIP2;1 with respect to metalloid uptake. The findings will expand mechanistic understanding of aquaporin's metalloid selectivity and facilitate variant interpretation to develop novel alleles with preference for beneficial metalloid species and reducing hazardous ones.

Introduction

Metalloid uptake in plants has a direct physiological and developmental effect. The transport of metalloids from root to upper plant organs is guided by active and passive channels like aquaporins (AQPs), phosphate transporters, citrate transporters, and inositol transporters [1–4]. The passive channel AQPs are the major players in this pathway. The nodulin 26-like intrinsic proteins (NIP) a subfamily of AQP in plants, have been widely associated with the influx of hydroxylated metalloid species from the rhizosphere. The expression and localization pattern of NIP homologues drives metalloid trafficking and sync, leading to the transport of the beneficial compounds like silicon and boron to anther, grains, and leaves.

The AQP family in plants is functionally and structurally more diverse as compared to animals, almost more than 30 isoforms are present in each plant species [5]. Based on the primary sequences, plant AQPs have been categorised in five subfamilies namely, the plasma membrane intrinsic protein (PIP), the tonoplast intrinsic protein (TIP), NIPs, small basic intrinsic protein (SIP), and uncharacterized intrinsic protein (XIP) [6]. Among all these subfamilies, NIPs have gained wide interest in terms of characterization, classification, and structural elucidation [7] due to their involvement in the uptake of essential nutrients like Nitrogen, and metalloids like Boron (B), and silicon (Si). The metalloid transport thus had been largely associated with the presence of NIP homologs in plants [8]. Based on the protein sequence NIPs are further divided into three subgroups NIP-I, NIP-II, and NIP-III with characteristic solute transport properties.

Considering the functional diversity of metalloid permeable AQPs, our efforts were directed to study metalloid uptake mechanisms of OsNIP2;1 (a high-affinity silicon transporter) [9,10]. All metalloid oxoacids like silicic acid, arsenous acid and germanic acid share the same transporter for their uptake in plants [1,11,12] with variable physiological responses. While silicic acid, boric acid and selenites are beneficial to plants, arsenic, germanium, and antimony are toxic to living organisms [13]. Despite the importance of regulating metalloid uptake through aquaporins, very less work has been done so far in this area. Specifically, in the case of arsenic toxicity, the knockout of OsNIP2;1, seems like an obvious approach. However, this approach comes with counterproductive issues, as it also results in a deficiency of beneficial elements like silicic acid [1]. The conventional breeding approaches are also futile to disrupt the radial transport of arsenic due to lack of genomic variations in OsNIP2;1. Henceforth, the study will be fundamental for employing genome editing targets for manipulating metalloid transport through the AQP channels.

Recent success in crystallizing OsNIP2;1 [9,14], a candidate of the NIP-III subgroup, has opened opportunities to study metalloid transport and specificity differences among AQP homologs. The OsNIP2;1 crystal structure shares a conserved architecture with axially tetrameric arranged monomers, with each functionally independent monomer twisted in a right-handed bundle. Six helixes and two half membranes spanning conserved NPA loops constitute the framework for each monomeric pore. The structural organization of NPA regions creates positively charged macro dipole in pore which in parts with conserved arginine of selectivity filter assists proton exclusion [15]. The narrowest constriction in the pore is called the ar/R filter and is confined to steric specificity for solute transport. The OsNIP2;1 channel is wider than the AQP homolog in *E. coli.* and differs significantly from classical single-file water transport models especially in the extracellular half, allowing more area for larger solute uptake [9].

Plant NIPs exhibit differential substrate affinity despite having similar pore sizes thus, the chemical properties of residues must be involved in this aspect. Surgical engineering of this transporter thus has the conundrum solving potential but will require atomistic details given the identical size, polarity, and hydrogen bonding capability of the substrate metalloids. Several previous studies focused on the ar/R selectivity filters of NIPs to comprehend metalloid specificity [16,17]. However, these studies alone did not provide an adequate explanation for substrate selectivity. In the present study, we have identified the pore-lining residues that are involved in silicic acid and arsenous acid uptake specifically, and a site-directed mutagenesis analysis was performed in yeast to test the importance of critical residues required for metalloid transport. A few selected mutants showed intermediate level of arsenic accumulation as compared to wild type OsNIP2;1. Such mutants will be helpful in reducing arsenic uptake while maintaining silicon accumulation in plants. Furthermore, the study has provided valuable insights into the solute specificity of aquaporins, specifically metalloid transporters.

Materials and methods

Molecular dynamics and simulation

Recently crystallized structures of OsNIP2;1 (Protein Data Bank (PDB) id. 7NL4 and 7CJS) were used for setting up initial stucture in the simulation studies. For modeling missing chain residues Alphafold predicted structure was used as a template in Modeller [18]. To develop the parameters for the metalloid, we optimized the metalloid molecular structure using Density functional theory (DFT) at B3LYP/LACVP level of theory. The optimized geometry was then used to calculate the charges using the RESP charge fitting method in gaussian [19]. Subsequently, frequency calculations were performed to determine the force constant. The Antechamber module of AmberTools20 was used to prepare the final parameters. The metalloids were found to be highly stable during the dynamics and showed expected non-covalent interactions with the protein residues. The OsNIP2-1 tetramer was buried in 65–70 POPC molecules in each leaflet of the membrane using CHARMM GUI membrane builder [20]. Respective metalloid was kept at 5 Å of the cytoplasmic opening of the AQP protomer. The simulation runs were carried out using CHARMM36 forcefield for protein and lipids and the TIP3P model for water in GROMACS simulation engine 2021 [21,22]. For confining a simulation box with periodic boundaries, the particle mesh Ewald method was applied. The timestep

for MD calculation was kept to 2 fs with a Vander wall cut-off of 12 Å distance. The charge on the system was neutralized by adding 0.5 M Na^+, Ca^{2+}, and Cl^- ions. Before implementing production runs step release equilibrations were done. First lipid tails were minimized and equilibrated for 0.5 ns. Constrain was slowly released from the system in successive steps and unconstrained equilibrium dynamics were done in final steps for 5 ns while maintaining substrate positioning at the channel opening. In the study classical simulations (1 us), Steered molecular simulations (5 ns) and adaptive biasing force runs (50 ns each window) were carried. Specifically, steered molecular dynamics (SMD) runs of 5 ns were done to study the transport pathway for protomeric channel with the careful selection of trajectories for obvious artifacts. The SMD runs were carried with a pulling velocity of 10 Å/ns. The random placing of the molecule on the pore opening could not show any permeation event and the molecules dissociated during the production run. So, the random shots from SMD simulations were used as start configurations for the potential of mean force (PMF) calculations. To determine the PMF of silicic acid and arsenous acid permeation along the channel, adaptive biasing force (ABF) method was used. Assuming metalloid translocation as a barrier crossing rare event like glycerol [23] dynamics of single-molecule was studied with respect to water and protein. Channel coordinates were divided into five overlapping segments of 5.5 Å each with a bin width of 0.1 Å. For ABF, the scaled spring constant of 400 kcal.mol^{-1}. A^2 was used on central silicon and arsenic atom restricted to a cylinder radius of 0.5 Å. The pore dynamics over the trajectory was studied using HOLE [24] along with VMD package [25] for molecular visualization and trajectory analysis. To assess convergence, we performed simulation analysis on at least three repetitions.

Cloning of rice NIP2;1 and site-directed mutagenesis

The open reading frame of *OsNIP2;1* was amplified from rice variety Pusa Basmati 1 using gene-specific primers flanked by NotI and XmaI sites (Table S1). The resulting PCR products were subcloned for functional protein expression in pYES2.1 (Invitrogen). To introduce point mutations in the coding sequence of OsNIP2;1, gene was cloned in the pJET1.2 vector. The overlapping primers with oligonucleotides flanking the target sites were designed to introduce point mutations. The bases of amino acids of interest were replaced by degenerate bases to generate diverse amino acid variations at the target site. The full-length pJET1.2 vector was amplified using Q5 DNA polymerase and subsequently cloned in *E. coli*. To confirm mutations at the target site, entire gene was sequenced using T7 and gene-specific primers. The selected mutants were digested using NotI and XmaI and subsequently cloned in pYES2.1 plasmid vector for yeast assays.

Yeast survival assay

Mutant for the FPS1 gene in Saccharomyces cerevisiae (BY4741 MATα his3Δ1 leu2Δ0 met15Δ0 ura3Δ0) were produced using the CRISPR-cas9 technique. In house developed fps1 mutant cured of cas9, was used for OsNIP2;1 complementation assays in yeast. The galactose-inducible pYES2.1 vector containing the URA3 selection marker was the vector of choice to express the OsNIP2;1. Yeast cells were grown on a synthetic yeast nitrogen base medium with ammonium sulfate containing 2% glucose or galactose at pH 5.5. The synthetic Complete Supplement Mixture (SC) w/o Uracil (URA) was supplemented for yeast transformant selection.

For functional yeast assay ΔFPS1 transformants were first grown on a primary culture with glucose, until A_{600} of 0.4–0.8 was reached. Cells from the primary culture were transferred to secondary media containing 2% galactose at a dilution of 0.1 and allowed to reach A_{600} of 0.6. Final dilutions of 0.1, 0.01, 0.001, and 0.0001 were spotted on YNB-URA plates with 2% galactose containing 3 mM sodium arsenite and 5 mM Germanium dioxide. For cytotoxicity growth assay, yeast cells were diluted to a initial OD_{600} of 0.01 in 30 ml liquid YNB-URA supplemented with 2% galactose. 2.4 mM of sodium arsenite was amended to the observation batch. The control and arsenite amended cultures were grown at 30 °C at 200 rpm and the OD_{600} was measured at the time lapse. All the yeast assays were performed thrice with biological replicates.

Quantification of arsenic accumulation

The arsenic accumulation of OsNIP2-1 variants transformed in ΔFPS1 was measured by ICP-MS. Yeast cultures were grown with 200 uM sodium arsenite to the OD_{600} of 1.0. The cells were centrifuged and pelleted with subsequent washing. The pellet was freezed at −80 for further lyophilization. The 10 mg of lyophilized cells were digested in 10 ml HNO_3 at 250 °C for 2 h. The digested concentrate was diluted to 5% and analysed by inductively coupled plasma–mass spectrometry ICP-MS.

Expression profiling of OsNIP2;1 variants

The OsNIP2;1 variants were cultured to an OD600 of 1.0 for RNA isolation and pelleted at 700 g for 5 min. Cells were homogenized using sonication at RT for 15 min. The plant RNA was extracted using RNAzol. The prepared RNA samples were treated with DNAse and quantified using nanodrop, spectrophotometer. The 1 ug of RNA was reverse transcribed using iscript cDNA synthesis kit. The final 1:10 dilutions were used for RT-PCR.

Results

Pore morphology of OsNIP2;1

In this study, crystal structure of OsNIP2;1 (7CJS) crystallized at 1.80 Å was used as a template. The stabilizing mutation for crystallization purpose was reverse mutated to WT sequence using CHARMM-GUI for further analysis. The simulation studies were found to be consistent with previous studies in terms of pore morphology [9,14]. The OsNIP2;1 has a wider overall pore radius as compared to classical AQPs and aquaglyceroporins (Fig. 1a). The narrowest region in the pore is ar/R (minimal radius ∼1.2 Å) located at a range of 5 to 10 Å and constituted of residues T65, S207, G215, G216, R222 [14]. At some instances the ar/R constriction was extended above 10 Å (Fig. 1a). This extended constriction was observed due to freedom of movement in S207 R group. It was found that in extended ar/R the Oγ atom of S207 was oriented towards the extracellular side (Fig. S1b). In contrast the inward facing S207 R group, leads to wider pore radius at 10 Å (Fig. S1c). These alternate conformers therefore propagate changes in location of ar/R and influence minimal radius of OsNIP2;1 as shown in Fig. 1a. Interestingly, our MD simulated protomers revealed another region of pore restriction present in the cytoplasmic half i.e., a minimum radius of ∼1.5 Å, (Fig. 1a, S2a, S2c). This region showed frequent side chain occlusions of H106, A105, T181, F115 and I96 choking cytoplasmic pore size of the channel. The H106 amino acid at this constrict was found highly conserved among 356 NIP class of AQPs (Fig.S4) [26]. Furthermore, the comparison of homology models of OsNIP1;2 (NIP-I), OsNIP3;1 (NIP-II) and OsNIP2;1 (NIP-III) suggests a wider diameter of extracellular vestibule for NIP-III. However, it is interesting to highlight that NIP-III has least inter-helix distance as compared to NIP-II and NIP-I (Fig. 1c). Hence the wider extracellular half is likely due to smaller

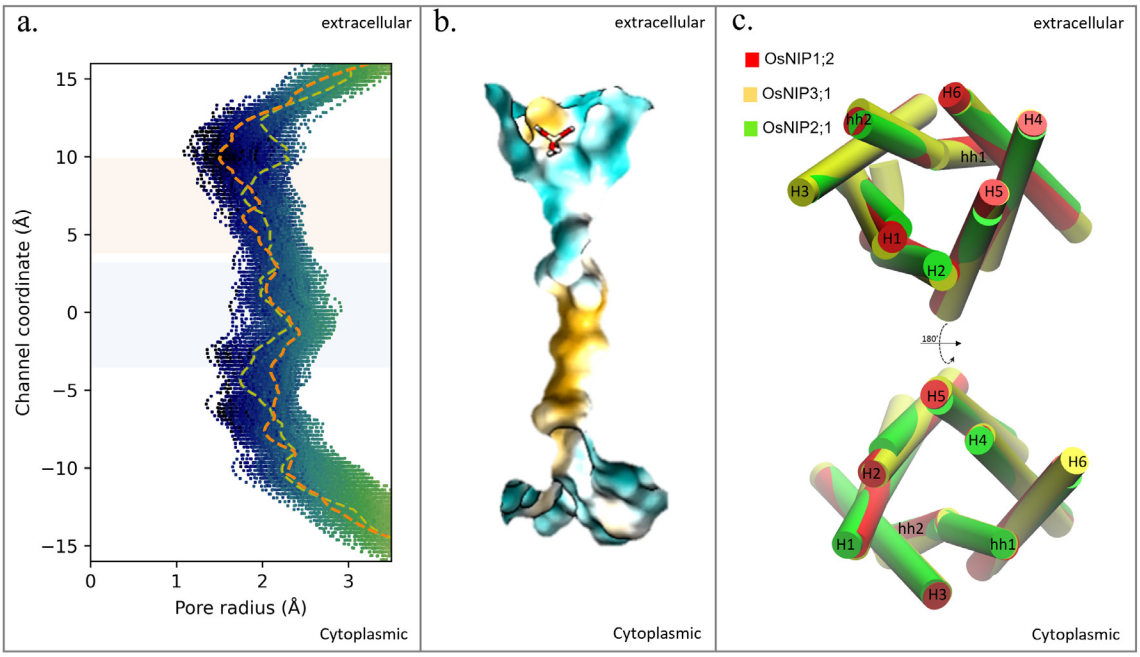

Fig. 1. Functional characteristics of OsNIP2;1 protomer (a) The HOLE radius was iterated for protomers of tetramer to illustrate the steric constricts. The profile was drawn from 1us trajectory. The size restriction sites of the simulated structure of OsNIP2;1 is mapped in dark colour. The highlights clearly show the localization of two-size constrictions in the pore at ar/R and cytoplasmic constricts. The variation in ar/R diameter for two conformers of S207 is apparent at 10 Å. The dotted orange line corresponds to S207 Oγ in outward facing conformation, whereas yellow line shows alternate inward facing conformation of S207 Oγ group. The different zones are shaded in orange for ar/R filter, and in blue for the NPA. (b) Longitudinal sections of protein channel showing hydrophobicity profile imposed by pore-lining residues is shown. Hydrophobicity is shown on sea green to orange shades indicating hydrophilic to hydrophobic amino acid distribution over the channel. (c) Comparison of helix positioning in alphafold predictions of NIPI (red), NIPII (yellow) and NIPIII (green) members in rice is represented. The more difference in extracellular face of protein i.e., top panel is clearly visible in comparison to cytoplasmic face (bottom panel).

residues packaging the pore (for instance GSGR selectivity filter) rather than helix packaging. In addition, the classical Aquaglyceroporin channels are characteristically hydrophobic in nature [27], however hydrophobicity distribution of OsNIP2;1 channel indicates adaptive evolution of extracellular half of NIP-IIIs to hydrophilic, probably to facilitate the transport of solutes like silicic acid (Fig. 1b, Fig. S3). The diversity in helix-helix distances, properties of pore lining residues and hydrophobicity, all suggests solute diversity to be attributed to extracellular vestibule of aquaporins (Fig. S3).

The Root Mean Square Fluctuation (RMSF) analysis of OsNIP2-1 simulations suggest that the loop regions of the channel are more dynamic than the intra-membrane helices. However, a short stretch in loop C elucidated restricted movement (Fig. 2a). The positioning of this loop forms a hydrophobic binding site for glycerol entry in the extracellular face of aquaglyceroporins [28]. In plant NIP AQPs, this loop is shortened, making a flap-like structure on the pore. Structurally the loop C was found to be held in position by the interaction between conserved G155, T157 and ar/R R222 residue (Fig. 2d, e, S4). This interaction explained the reason of low RMSF fluctuations in Loop C. Surprisingly, in some monomers spontaneous breakdown of G-R interactions was noticed, resulting in high RMSF values (0.82 Å) for loop C (Fig. 2a). The conformation deviation in this region, leads to Arg dihedral shift, consequently blocking the pore (diameter ~1 Å; Fig. 2b). Thus, structural stability, here provided by G-R interaction is required for correct positioning of R222, ensuring open state of the channel. In the attempt to confirm the computational predictions, we analysed OsNIP2;1 G155A mutant for arsenite and germanium dioxide (GeO_2) uptake. The transport activity of Germanic acid and arsenous acid was lost in the loop C mutant which indicates the functional impact of conserved G155 residue, and the proper positioning of loop C over the AQP pore (Fig. 2c).

Energetics of metalloid transport through OsNIP2;1

Cognizant of the low permeation frequency of silicon as compared to water, metalloid conduction was accelerated through external forces. The silicon and arsenic permeation was studied by steered molecular dynamics simulations. Since the AQP channels are passive bidirectional transporters, the channel was analysed for the import as well as export of metalloids. Many reports from in silico and in vitro results highlight the importance of ar/R filter in solute specificity [17,23,29–32]. Our results supported the significance of the ar/R filter in determining solute specificity. Specifically, the force analysis of silicon transport showed that the ar/R filter exhibited a maximum force of 249.92 pN for import, while the export peak had a force maxima of 187.59 pN at ar/R (Fig. 3b). In addition, examination of the channel's radius indicated steric restrictions in the cytoplasmic half (as demonstrated in Fig. 1a and 3a), which were further supported by permeation energetics (Fig. 1a, 3a). The Force profile showed two major peaks in the cytoplasmic half of the channel for silicic acid. These peaks of 220 pN and 210 pN were traced to −7 Å and −10 Å, respectively, and were associated with the size restriction imposed by residue T181, V199 and F115 (Fig. 3a). Silicon transport also indicated high force requirement in the Loop C region i.e. 10 to 15 Å (Fig. 3b) which is probably due to the orientational restriction for metalloid molecule for successful entry into the channel pore.

Regarding the SMD profile of arsenous acid, the largest force peak was consistently at the extracellular half, with a maximum of 258 pN for import and 325 pN for export. The location coincides with the position of the ar/R filter. However, the apparent divergence in force profile at the cytoplasmic constrict was found between silicic acid and arsenous acid. The influx of silicic acid showed a maximum of 221.25 pN however for arsenous acid the regional value corresponded to 77.9 pN. It can be due to the fact

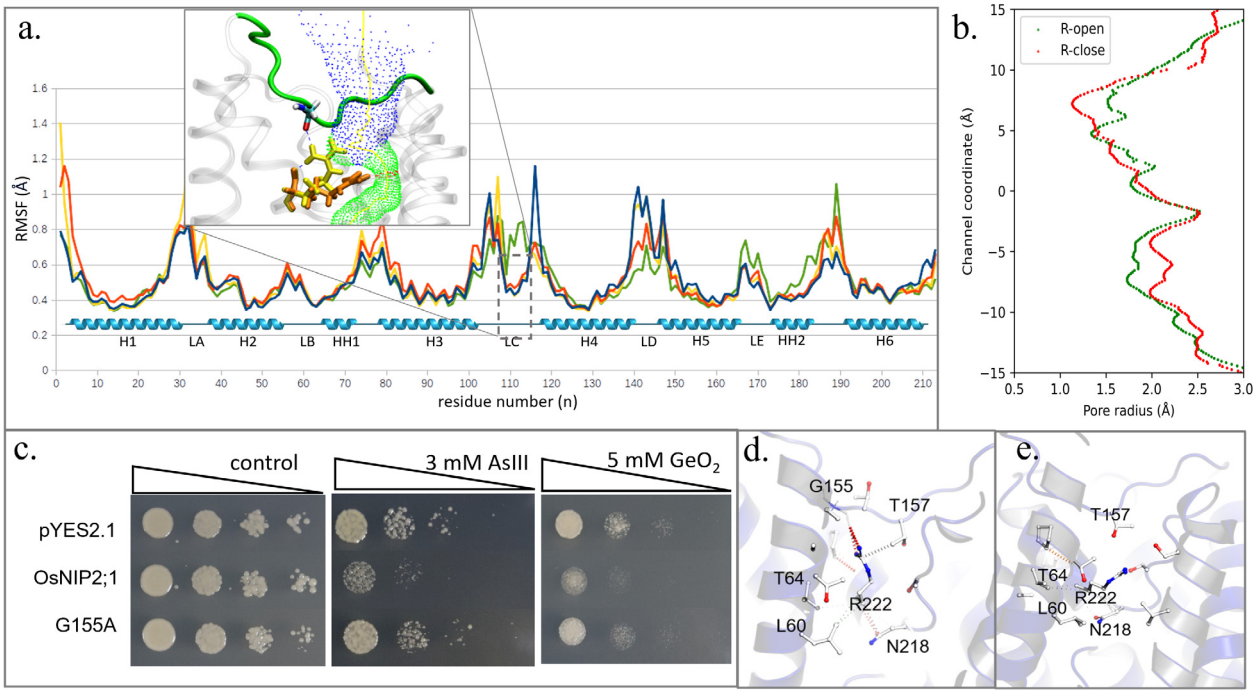

Fig. 2. Structural influence of Loop C in metalloid permeability (a) Root mean square fluctuations superimposed for OsNIP2;1 monomer is shown. Prominent structural deviation for loop C is visible in the green plot. This leads to a consequential change in the structure of residue R222, which can be observed from the zoomed-in panel. The intact G-R interactions are represented in yellow for Arg, while the altered Arg orientation is shown in orange shade. (b) The illustration demonstrates the impact of different arginine conformations on the channel radius of OsNIP2;1. (c) The yeast complementation assay was conducted to assess the functional influence of loopC residues. As compared to the wild-type, loop C G155A variant showed a decrease in metalloid uptake. (d) The hydrogen bond network of G155 and T157, attracts R222 of SF, thereby keeping the pore in open state. Conversely, the breakdown of this interaction reduces the pore size of SF, resulting in a more closed state (e).

that silicic acid has a wider overall diameter of around 6 Å with one extra hydroxyl side chain and thus is influenced by cytoplasmic restriction more than the smaller-sized arsenous acid. Across the NPA regions force, peaks were around a minimum of 50 pN illustrating an energetically favourable state for the solute molecule. The OsNIP2;1 channel displayed comparable peak magnitudes for both import and export of the metalloid, indicating bidirectional transport capability. However, the wider hydrophilic outer half of OsNIP2;1, may promote metalloid import by facilitating better hydration of molecules. (Fig. 1b, a).

Aware of the fact that SMD simulations do not allow conformational relaxation to protein backbone, bidirectional metalloid permeation was investigated by adaptive biasing forces, using system coordinates from SMD trajectory. The z coordinate of tetrameric protein system was divided into five windows of 5.5 Å each with an overlap of 1 Å to adjacent window (Fig. S5). The random snapshots of the molecules from SMD were used to define initial coordinates for each ABF window. A combined PMF was plotted against z coordinates to define free energy over the OsNIP2;1 channel. The convergence was further cross checked by PMF of overlapping windows. The comparison with SMD profile showed overlapping energy barriers for both the estimations.

The potential mean force profile showed consistent major peaks of 2.5 kCal and 2 kCal at the ar/R region for silicic acid and arsenous acid respectively (Fig. 3c, e). Similar to the force profile, the second peak of 3.13 kCal was localized to the cytoplasmic choke for silicic acid. However, for arsenous acid, the positional equivalent peak was recorded at 1.11 kCal thus supporting an additional restriction site in the cytoplasmic half for the silicic acid. Owing to the low permeation of metalloids as compared to water, a prominent peak is also evident at loop C position i.e., around z = 12.32 Å. Multiple other small barriers are featured in the channel indicating local binding of metalloid substrate to channel residues, solute orientation, limited sampling, and constrained protein backbone required to limit system drifting in the z direction.

Prediction of pore lining residues involved in metalloid transport

In coherence with the water uptake pathway, the hydrogen bond relay [33] is the mechanism for the passive transport of metalloids through NIP channels. Thus, to understand the critical molecular interaction between the metalloid molecule and amino acids constituting pore, hydrogen bond (H-bond) network from steered molecular dynamics permeation events was calculated (Fig. 4c). The analysis of H bond interactions between metalloids and channel lining residues complements PMF and SMD results. Interestingly, the major proportion of H-Bonds was localized to ar/R, NPA, and cytoplasmic constrict (Fig. 4b, c). Hydrogen bonding with residues forming steric restriction sites in the extracellular half and cytoplasmic half were highest. As shown in Fig. 3f the residence time for silicic acid as well as arsenous acid is higher at 5 Å and −7 Å corresponding to the ar/R and cytoplasmic restriction site. The retention time of silicic acid at cytoplasmic constrict was relatively more than the arsenous acid (Fig. 3f), again reinforcing the selective steric choke for bulkier silicic acid in cytoplasmic half of OsNIP2;1.

The ar/R selectivity filter of OsNIP2;1 is known to be constituted of T65, G88, S207, G216, and R222. Surprisingly, G88 at the second helix position was found to be minutely involved in hydrogen bonding with metalloid (Fig. 4b). Another residue, Q84 located in the same helix had comparatively more H-bond involvement with metalloid species facilitating metalloid transport (Fig. 4b). The S207 residue at the fifth helix was highest involved in solute channelling indicating an interesting candidate for manipulating metalloid specificity. The confirmation flexibility to S207 might be corresponding to the high importance of H5 serine in metalloid

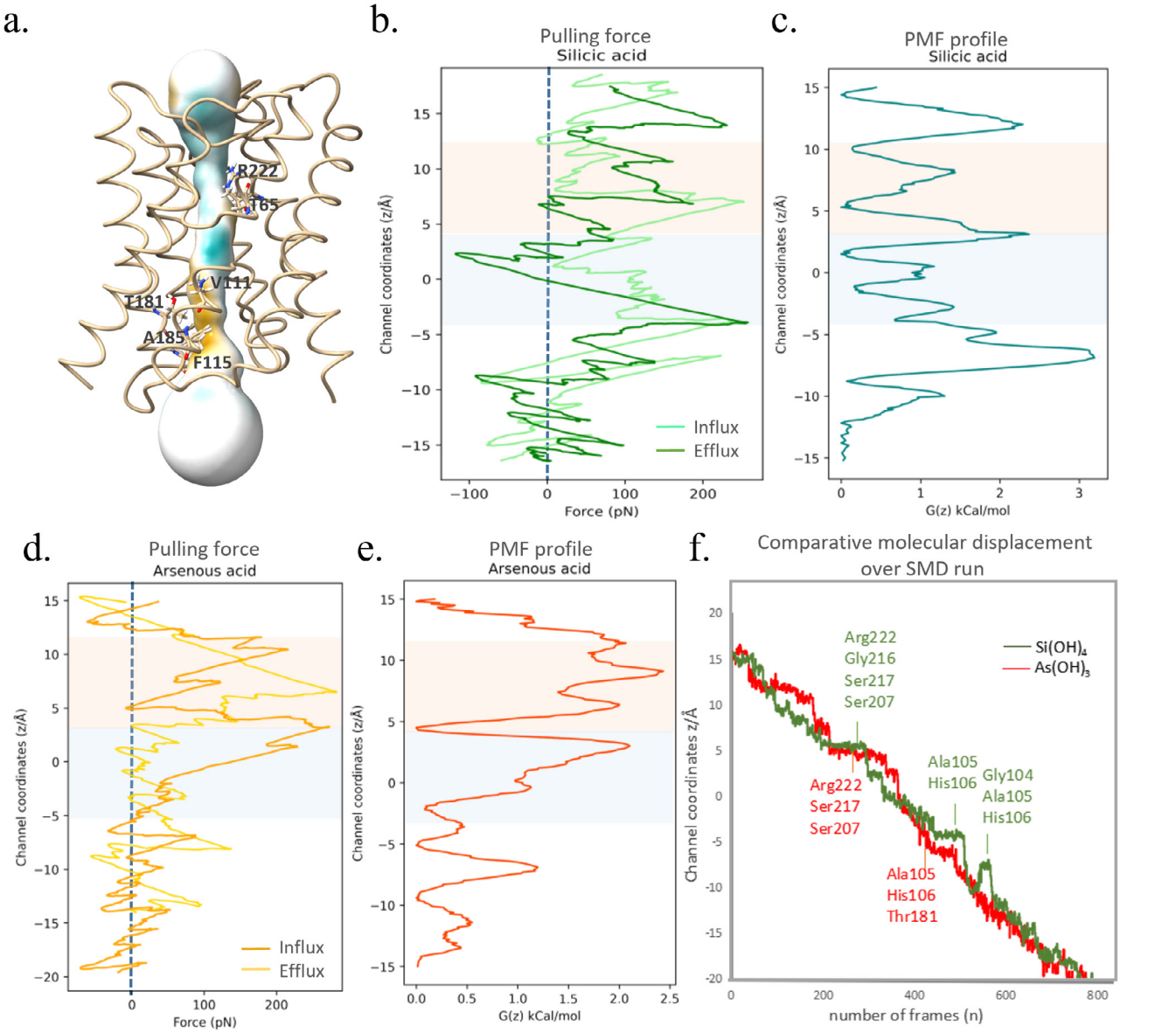

Fig. 3. Metalloid interaction energy across the OsNIP2;1 channel. (a) The residues closest to two predicted constricts, based on radius profiles, are highlighted in the map. The force required to transport silicic acid and arsenous acid through the functional pore of OsNIP2;1 is plotted as running averages in graphs (b) and (d), respectively. The higher peak in the graphs coincides at size exclusions plotted against the normal (z) of the protein. The zero position is located at the geometric centre of a protomer i.e. the NPA region. The potential of mean force (PMF) for silicic acid and arsenous acid transport, relative to the protomer z-axis, is represented in (c) and (e), respectively. The relevant zones are color-coded in orange for ar/R filter and blue for the NPA. (f) Moreover, the relative residence time for silicic acid and arsenous acid during metalloid uptake is evaluated to map time limiting regions of the channel.

permeable aquaporins (Fig.S1) [17]. Notably, the H5 position shows S/I variation among NIP-II and NIP-III classes of AQPs, switching selectivity filter hydrophilic/hydrophobic. At the NPA region in OsNIP2;1 both asparagine residues (N108 and N219) were predominant interactors followed by 215GGS and 104GAH amino acids, that physically flank NPA residues. Although G216 is the residue occupying selectivity filter position on a sequence alignment basis, other residues G215 and S217 also showed H-bonding with metalloid species dynamically (Fig. 4b, c).

Validation of predicted residues in yeast ΔFPS1 mutant

To elucidate the physical relevance of predicted residues in metalloid uptake, yeast survivability assays were performed. For developing yeast strain mutant for metalloid uptake, the host metalloid transporter *FPS1* gene was targeted using CRISPR/cas9 mutagenesis. The sgRNA was designed near 318 bp of start codon (Fig. S6a, Table S1). The synthesized sgRNA was cloned in the pML104 vector between BclI and SwaI sites. The final construct was transformed in BY4741 (MATα *his*3Δ*1 leu*2Δ*0 met*15Δ*0 ura*3Δ*0*) strain. The URA rescued transformants were screened on 5 mM AsIII to select FPS1 knockout mutants. The colonies growing on an otherwise lethal concentration of arsenite were sequenced for FPS1 gene editing. Mutants were found to have frameshift mutation by the insertion of single bases in FPS1 (Fig. S6b). For vector curing, edited cell lines were grown on non-selective media and were replica plated for 12 generations on SD URA and YPD plates. The colonies unable to grow on SD URA after generations were reconfirmed for loss of plasmid using PCR amplification. The selected mutant was used in the study for gene complementation (Fig. S6c).

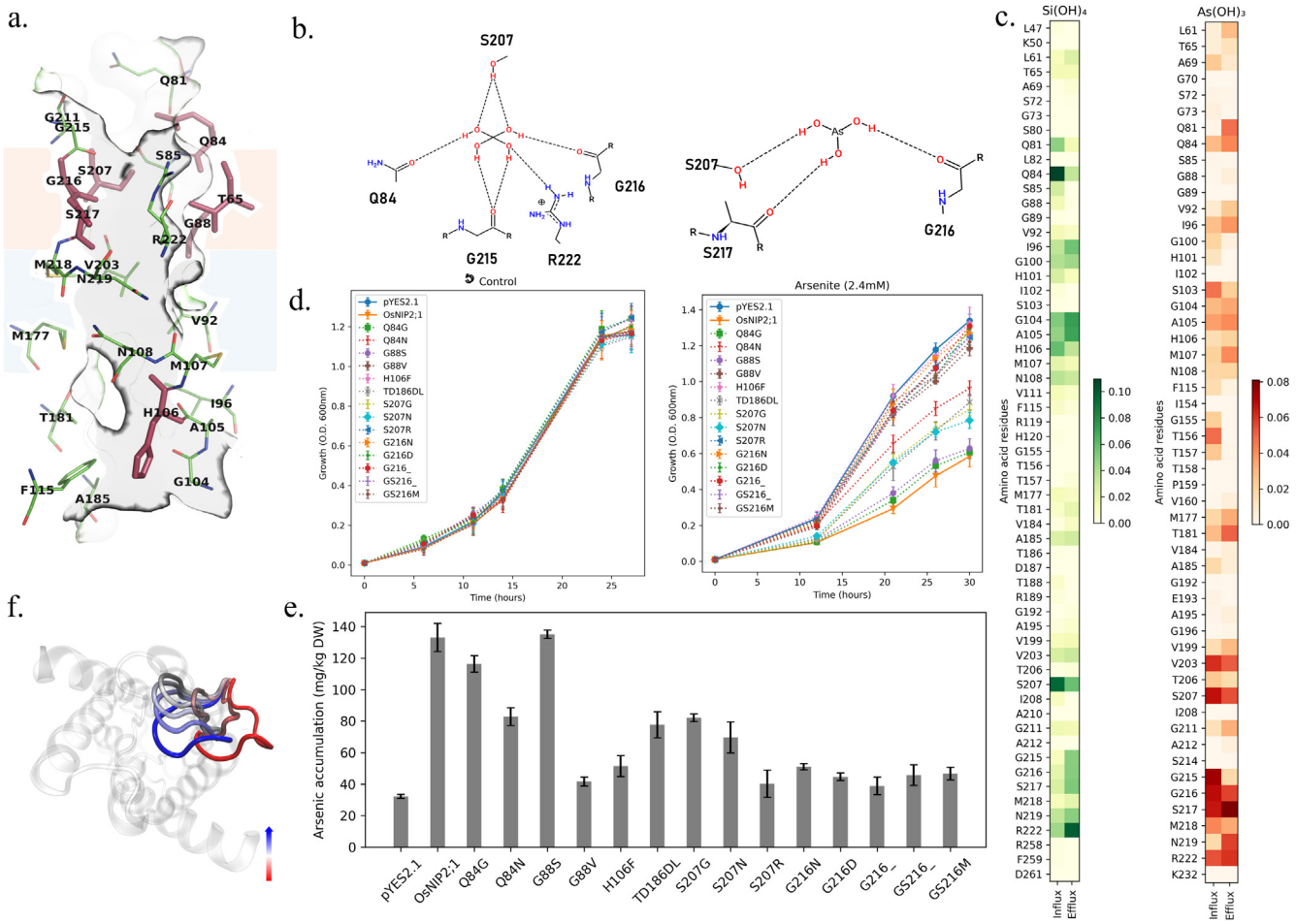

Fig. 4. Metalloid-Channel contacts (a) The permeation path of OsNIP2;1 and its constituent residues are labelled. (b) The major interactions at ar/R for silicic acid and arsenous acid from the trajectory frame are highlighted. (c) The contribution of each residue to the total permeation of silicic acid (green) and arsenous acid (red) is shown in a gradient scale. (d) Cell viability of the fps1Δ mutant expressing empty vector, OsNIP2;1, and various site-directed mutagenesis variants were assessed under control and 2.4 mM As(III) amendments. (e) The same set was subjected to treatment with 200uM As(III) until an OD600 of 1.0 was reached, and arsenic accumulation was determined by inductively coupled plasma mass spectrometer (ICP-MS). (f) The variation in the conformation of loop D over a 100 ns trajectory is illustrated, with the loop colour-mapped from red to blue to show the simulation transition from an open 7CJS-like state to a closed 7NL4-like state.

To identify functionally important residues within pore channel, residues with predicted high contribution for metalloid permeation i.e.T65, Q84, G88, S207, G216, H106 (Fig. 4a, b, c) was mutated using degenerate primers. A collection of generated mutants along with wild type strains were cloned in pYES2.1, yeast expression vector. The membrane localization of OsNIP2;1 was confirmed by confocal microscopy (Fig. S7e). Furthermore, The expression of lsi1 variants was assessed by RT-PCR in yeast subjected to 2% galactose (Fig. S7d). The yeast cells expressing OsNIP2;1 variants grown in 2.4 mM AsIII showed reduced growth as compared to yeast cells with wild type (WT) allele (Fig. 4c, d). Growth assay illustrated three groups of response to arsenic cytotoxicity (Fig. 4d). Some variants like G88S and Q84G had very minute effect on arsenic uptake and were equally sensitive to sodium arsenite dosage. Other group having deletions at crucial positions (G216, S217), substitution by bulky amino acid (G216N, G216D) or substitution by amino acid with opposite chemical properties (H106F, G88V), showed complete loss of arsenic uptake. The arsenic resistance in these mutants can be attributed to structural anomalies aroused in pore regions. Interestingly, a few mutants like Q84N, S207G, S207N with intermediate arsenic sensitivity was observed. This group had cell survivability between the OsNIP2;1 complemented cells and FPS1 knocked out mutant in 2.4 mM arsenite. Interestingly, these mutants retained Germanic acid uptake capability (Fig. S8), representing silicic acid uptake characteristic of OsNIP2;1.

The level of arsenic accumulation in these variants was also measured by ICP-MS. The OsNIP2;1 mutants were cultured in 200 uM sodium arsenite concentration and 10 mg cell pellet was digested for arsenic quantification. The mean cellular arsenic accumulation concentrations was found to be 32.22 ± 1.07 mg kg–1 for empty vector and 133.04 ± 2.40 mg kg–1 for yeast cells transformed with WT OsNIP2;1. The mutants with intermediate level of arsenic sensitivity in cytotoxicity assay showed a reduction of 37.75 to 47.64 percent as compared to wildtype OsNIP2;1 (Q84N (82.81 ± 4.47 mg kg–1), S207G (82.18 ± 0.77 mg kg–1), S207N (69.65 ± 9.91 mg kg–1)) (Fig. 4f). The arsenic concentration in Q84G(116.32 ± 1.42 mg kg–1) and G88S (135.07 ± 1.54 mg kg–1) mutants was slightly decreased but the difference was not significant. Certain mutants showed highly reduced arsenic uptake, which possibly suggests that the protein pore of these variants is non-functional. (Fig. 4F).

At the cytoplasmic exit site, T186 and D187 residue from loop-D of neighbouring protomer was found to interact with metalloid species minutely. Both residues show high conservation in loop-D among all three classes of NIP aquaporins (Fig. S8). Interestingly, in the available two crystal structures for OsNIP2;1 the orientation of loop-D is variable that gates pore in open and closed conforma-

tions. In our study, we isolated a double mutant TD186DL from degenerate base library that showed resistant to arsenic uptake (Fig. 4d, f, S6). To elucidate the inference of mutation, simulation on wild-type OsNIP2;1 TD186DL, T186D, and D187L were carried for 100 ns. To complement our yeast assay, the double mutant TD186DL illustrated destabilization of open conformation shifting loop-D to closed state (Fig. 4e, S7) as found in the 7NL4 crystal structure.

Molecular orientation for metalloid transport

The known metalloid substrates of NIP aquaporins exist in either planar trigonal, trigonal pyramidal or tetrahedral geometry. This compact symmetric orientation along with hydroxyl corners allows metalloids to enter the plants using AQP channels. To understand the molecule's behavior inside the channel, orientations of different metalloids along OsNIP2;1 channel were studied. The ±θ value was calculated as a measure of the real-time angle between the molecule's principal axis (v) with respect to membrane normal (z), hence a value closer to 90 signifies parallel orientation to the pore axis whereas a lower value indicates perpendicular state. Similar to glycerol, uptake of planar molecule arsenous acid through OsNIP2;1 channel was confined to parallel orientation with respect to the z-axis (Fig. 5a). However, tetrahedral molecular symmetry for $Si(OH)_4$ gives the advantage of one extra hydroxyl group to this molecule, hence no strict orientation pattern was there for silicic acid. For both water and glycerol, the two NPA half helices provide positively charged dipoles that reorient water molecules at the centre of the channel. This reorientation was also observed for arsenous acid and silicic acid (Fig. 5a, 5b). From the observation it is clear that the dipole orientation of protein's extracellular and intracellular half is responsible for this behaviour and it should be consistent for all neutral substrates of AQP [15,28,34,35]. We also observed the influence of hydrophobicity of ar/R on the orientation of arsenous acid. In OsNIP2;1 where the selectivity filter is composed of TGSGR, the hydroxyls of arsenous acids were oriented to S207 and the residue was directly involved in metalloid uptake (Fig. 5c) but in case of AtNIP5;1 (AIGR) H5 position is occupied by hydrophobic I236. For AIGR the arsenous acid was found oriented in a manner that hydroxyls face away from hydrophobic I236 residues (Fig. 5d). In addition the metalloid-water coupled movement also showed a transient break in water movement through the channel during metalloid passage thus ruling out co-permeation of silicic acid and water molecules at a time from the same channel.

Discussion

Protein sequence conservation analysis performed in diverse organisms suggests that the plant AQPs have undergone functional divergence during evolution, attributed to ecological and evolutionary advantages for adaptation to the local environment [36–38]. Among the five major subfamilies of AQPs, plant NIPs have evolved with very high solute specificity. Even within NIPs, three groups (NIP-I, II, and III) have evolved specific absolute specificity and fine-tuning of solute transport. Understanding of factors defining the solute specificity will allow desired modification in AQPs which has wide application in health, medicine, environment, and agriculture. The present study examined the structural features of OsNIP2-1 relative to the metalloid uptake property of these channels. It is difficult to ascertain permeation events in a shorter time scale because of a lower rate of metalloid uptake and high configuration barriers. In addition, the orientational restrictions also limit coupled movement of two silicic acid molecules in the pore. Thus, steered dynamics approach was employed to collect energy information during the passage of a molecule through the pore of OsNIP2;1.

The AQP is made up of two symmetrical halves that extend across the membrane, with one half inverted relative to the other. The cytosolic half of the AQP is more conserved in terms of sequence than the extracellular-facing half. As a result, the extracellular half of AQPs exhibits greater diversity and contains a selec-

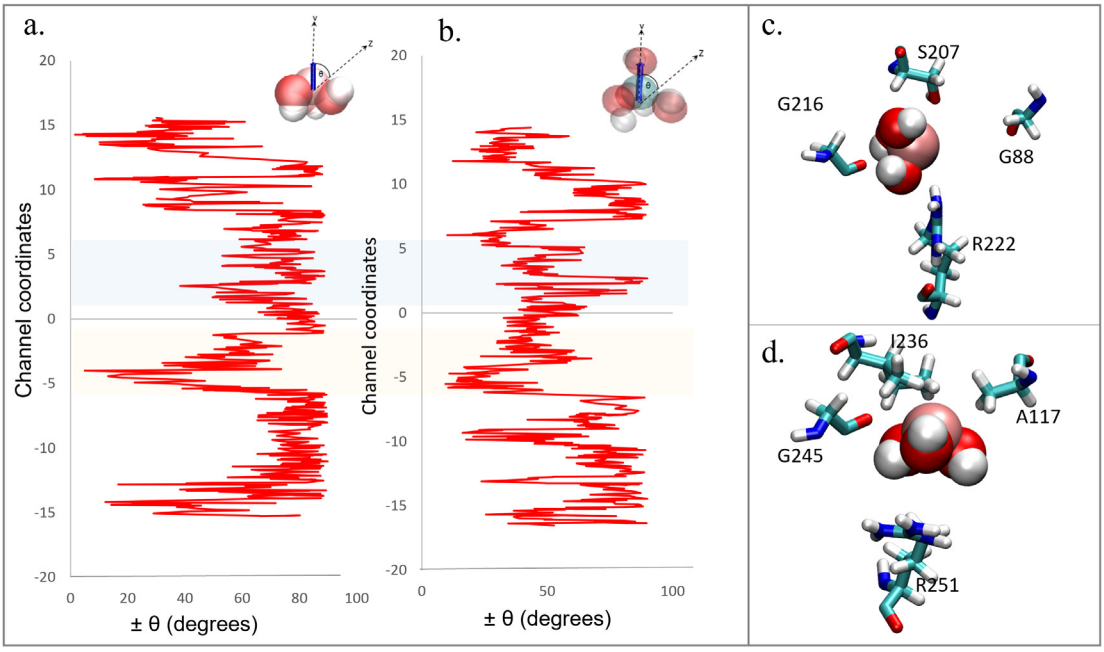

Fig. 5. Orientational dynamics of arsenite (A) and silicic acid (B) through OsNIP2;1. The θ value was calculated between 0° to 90°. The principal axis of the molecule is represented in a blue arrow on the side panel for silicic acid and arsenous acid each. The NPA and SF position is highlighted in blue and orange. The comparison of arsenous acid molecule traversing through selectivity filter of OsNIP2;1 (C) and AtNIP5;1 (D). The influence of hydrophobic residue in the SF is evident from arsenous acid hydroxyl reorientation in the AtNIP5-1 selectivity filter.

tivity filter called ar/R. Structural analysis of OsNIP2;1 reveals that its selectivity filter consists of TGSGR [9,14] with an ar/R radius of 1.8 Å (Fig. 1a). Dynamically this constriction site showed a minimum radius of 1.2 Å over the simulation trajectory regulating size restricted solute specificity of OsNIP2;1. The interplay of hydrophobicity with reference to solute uptake has not been addressed so far in plant aquaporins. The protein sequence analysis for NIP family aquaporins shows that the extracellular half of the OsNIP2;1 shows more hydrophilic behaviour as compared to the cytoplasmic half facilitating the uptake of hydroxyl molecules (Fig.S3). Moreover, OsNIP2;1 channel's less permeability to glycerol is further explained by the polar hydrophilic extracellular half [1]. The selectivity filter for OsNIP2;1 is hydrophilic and hydrophobic substitutions in this constriction had detrimental effects on metalloid uptake. In our study substitution of G88 at the H2 position with serine did not affect arsenic or germanium dioxide uptake but the incorporation of hydrophobic valine at the same site restricted arsenic and germanium uptake. Similarly, a previous report found little effect on G88A substitution on arsenic uptake [17]. We also found a significant impact of S207 mutation on solute uptake. In our study, all of the mutations at the H5 site showed a detrimental impact on metalloid uptake (Fig. 4c, d, f). The critical importance of this H5 position is further illustrated by the maximum contribution of S207 in metalloid-protein hydrogen bonding interaction (Fig. 4c). This property was attributed to better R group flexibility of S207. Over the simulation run, the S207 R group acquired two alternate conformers, allowing a longer metalloid-S207 interaction period. Interestingly this position is also a potential candidate for substrate specificity difference among NIP-II and NIP-III AQPs. The presence of a hydrophobic I236 in the selectivity filter of AtNIP5;1 was found to reorient the molecule in a manner so that hydroxyl side chains of metalloid were pointing away from hydrophobic residue whereas positional equivalent S207 in OsNIP2;1 favours hydrogen bonding of metalloid hydroxyls (Fig. 5c, d). Thus the difference in hydrophobicity can explain low permeability for four hydroxyls containing orthosilicic acid among NIP-II class of AQPs with AI/VGR selectivity filter. The observations suggest that the ar/R serves a dual filter for hydrophobicity and size exclusion in metalloid permeable aquaporins. Apart from that the loopE selectivity filter residues G215, and G216, along with S217 were found structurally important and are significantly involved with metalloid species (Fig. 4b, c). Hence, a dynamic behaviour must be considered for metalloid tuning of this site. Simulation studies also revealed the involvement of a Q84 residue which contributed significantly to silicic acid uptake. A previous study in anther specific boric acid transporter AtNIP7-1 also showed modulation of solute specificity upon Y81F mutation which occupies the same position on alignment [39]. The two-half helix protruding NPA amino acids to the protein geometric centre is the characteristic feature of AQPs. During metalloid transport, Asparagine side chains in NPA directly interacted with OH side chains and were critical in the reorientation of the molecule at the centre of protein (Fig. 5a, b). Our ICP-MS analysis of OsNIP2;1 mutants for ar/R siteexpressed in yeast cells highlighted three interesting candidates with reduced arsenic uptake. These variants named S207G, S207N and Q84N had considerable reduction in arsenic accumulation along with decreased germanium dioxide sensitivity. These features suggest maintenance of silicon transport activity of OsNIP2;1 while reducing cellular arsenic levels.

Apart from selectivity filter, chemistry of residues lining the pore provide special adaptations to protein. The cytoplasmic half of the protein is shown to regulate pore conductance in accordance to physiological state. These gating are regulated by ionic binding, protein–protein interactions, and phosphorylation [40]. In case of OsNIP2;1 the general understanding of the cytoplasmic half in solute specificity has only received a scant amount of research. However, based on the features of OsNIP2;1, a second constrict having a minimal radius of $\sim$ 1.5 Å is prominent in the cytoplasmic half (Fig. 2b). The major residues contributing to metalloid binding in this second constrict involved T181, F115, A185, H106 (Fig. 4a) and are largely conserved among NIPs especially H106 (Fig. S4). In our study, this cytoplasmic constrict created a more pronounced bottleneck for silicic acid. The lack of hydrogen donors in this region of the channel due to higher local hydrophobicity and size constriction might be the two reason for higher energies and retention times for silicic acid (Fig. 4). Overall force and free energy profiles for silicic acid and arsenous acid transport through OsNIP2;1 showed similar energy barriers. The free energy profile showed three prominent peaks for metalloid permeation one at loop C, one near the ar/R filter, and one in the cytoplasmic constrict (Fig. 3b, 3d). The high peak in the ar/R region is common for AQPs and numerous reports suggest the same [23,29,30] but the presence of additional barriers in the cytoplasmic region is unique to OsNIP2;1 and we believe for most of the NIP-III family aquaporins. An earlier report [10] discussed a peak corresponding to 8.4 ns retention time in the 0 to −10 Å region. Similarly, QM/MM simulations [9] also showed a broad bottleneck for silicon density in the cytoplasmic half thus, reinforcing the prospect of size exclusion in the cytoplasmic half as well. Also, the magnitude of cytoplasmic constrict PMF for bulkier silicic acid (5 kCal) was more than the arsenous acid (3 kCal). Overall energy profile suggests metalloid pore interactions and steric chokes to be responsible for energetic barriers along permeation pathway.

Numerous studies on AQPs have shown the effect of structural elements other than pore-lining residues in solute specificity. The loops especially play a critical role in solute binding and influence gating of AQPs [41–46]. We functionally characterized two novel sites i.e. G155 and TD186 situated in loop C and loop-D respectively to have a direct influence on metalloid transport. The G155 was found to hold R222 in an upright state leaving pore in open conformation. The breakdown of this interaction shifted R222 into a pore occluding closed state (Fig. 2d). The arginine in ar/R filter has long been debated for gating among other aquaporins [4748,49]. But the influence of loop C-R interactions must be more prominent for NIP-III aquaporins since the extracellular vestibule is comparatively more wider having extra space for arginine side chain movement. With the increasing evidences of role of extracellular loops in cell cell adhesion and signalling [50,51], the factors that might control loop C dynamics of NIP class aquaporins remain to be illuminated. In addition, Arginine dihedral shift comprise an interesting mechanism to alter aquaporin functionality by metal ion binding [52], loop C dynamics [51] and ar/R filter residue variations [39,53].

The conformation of loop-D differs in closed and open state in two reported crystal structures of OsNIP2;1 i.e. 7NL4 and 7CJS. The only dissimilarity in open state is the binding of a Na^+ ion to loop-D crystal lattice (Fig.S7a). In our study, we were able to replicate loop-D closed state as seen in the 7NL4 crystal structure by mutating T186 and D187 residues of OsNIP2;1. This finding unravel precise networks in residues, which indirectly contribute to functionality of channel and modulate solute permeability. Collectively, these modulatory sites elucidate the knowledge gap that remained in functionality and regulation of NIP class aquaporins. For instance, only a single report had characterized OsNIP2;1 phosphorylation so far [54]. Also, a recent study has shown GF-14f and ATP synthase a subunit interacting to OsNIP2;1 using Co-immunoprecipitation and biofluorescence complementation [55]. A possible way of gating OsNIP2;1 is through phosphorylation-mediated binding of GF14f to its N or C terminals. A previous report suggested the interplay of $HgCl_2$ in loop-D shift [56] however this seems unlikely because reduction of OsNIP2;1 might be

due to Hg2+ ion binding at C66, mimicking mercury sensitivity of AqpZ [52]. Although the effects of phosphorylation, pH, ionic binding, and protein–protein interaction remained in infancy for NIP structure–function relationships, previous insight from gating mechanisms of SoPIP2-1 and AQP2 can serve as models for NIPs which will help to bridge the knowledge gaps. All these novel structural features like wider pore radius and hydrophilic extracellular half of NIPs, are pointing towards metalloid-specific neofunctionalization of these aquaporin channels. Furthermore, the comparison of the steric consensus structures of metalloid substrates reveals that the smaller size and favourable hydrogen bonding pattern of arsenous acid enable it to pass through NIP-III and NIP-II channels in a non-selective manner (Fig. S10). Our results suggest that it might not be feasible to completely inhibit arsenous acid without impacting silicic acid uptake. However, since silicon is a beneficial but non-essential element, the presence of weaker alleles with lower affinity for metalloid substrates provides a potential avenue for breeding rice cultivars with low arsenic levels.

Conclusion

The present study provides the first energetic landscape of silicon and arsenic permeation through OsNIP2;1. We were able to highlight structurally and functionally critical residues for metalloid transport of aquaporins. The results reveal steric barriers to improve silicon uptake in NIP class aquaporins. Consistent with the widespread NIP homologues in the plant kingdom, and relatively lower selectivity for arsenic among NIPs, our study identified OsNIP2;1 variants having intermediate level of arsenic accumulation. Due to abundance of silicon in most of the soil such weaker alleles of OsNIP2;1 might be crucial for developing low arsenic rice cultivars.

Compliance with Ethics Requirements

This article does not contain any studies with human or animal subjects.

CRediT authorship contribution statement

Yogesh Sharma: Data curation, Formal analysis, Methodology, Writing – original draft. **Vandana Thakral:** Methodology. **Gaurav Raturi:** Methodology. **Kshatresh Dutta Dubey:** Software, Validation. **Humira Sonah:** Writing – review & editing. **Ashwani Pareek:** Writing – review & editing. **Tilak Raj Sharma:** Writing – review & editing. **Rupesh Deshmukh:** Conceptualization, Funding acquisition, Investigation, Project administration, Resources, Supervision.

Declaration of Competing Interest

The authors declare that they have no known competing financial interests or personal relationships that could have appeared to influence the work reported in this paper.

Acknowledgment

The authors are thankful to the Department of Biotechnology (DBT), Government of India (GoI) for the Ramalingaswami Fellowship Award to HS and RD; Grant BT/PR32853/AGII I/103/1159/2019, BT/NIPGR/Flagship-Prog/2018-19 and Grant BT/PR38279/GET/119/351/2020 to HS, RD and TRS; The Science and Engineering Research Board (SERB), India, Department of Science and Technology (DST), Government of India (GoI), for JC Bose Fellowship to TRS, and Research grant CRG/2019/006599 awarded to RD, HS, and TRS; Council of Scientific & Industrial Research for Junior research fellowship to YS, VT. We acknowledge National Supercomputing Mission (NSM) through Centre for Development of Advanced Computing (C-DAC) of the Ministry of Electronics and Information Technology (MeitY), government of India, for providing the support of high-performance computing.

Appendix A. Supplementary material

Supplementary data to this article can be found online at https://doi.org/10.1016/j.jare.2023.04.020.

References

[1] Ma JF, Tamai K, Yamaji N, Mitani N, Konishi S, Katsuhara M, et al. A silicon transporter in rice. Nature 2006;440(7084):688–91.
[2] Ma JF, Yamaji N, Mitani N, Tamai K, Konishi S, Fujiwara T, et al. An efflux transporter of silicon in rice. Nature 2007;448(7150):209–12.
[3] Sanz A, Novacky A. Evaluation of arsenate-and vanadate-associated changes of electrical membrane potential and phosphate transport in Lemna gibba-GI. J Exp Bot 1989;40:119–28.
[4] Duan G-L, Hu Y, Schneider S, McDermott J, Chen J, Sauer N, et al. Inositol transporters AtINT2 and AtINT4 regulate arsenic accumulation in Arabidopsis seeds. Nat Plants 2015;2(1):1–6.
[5] Maurel C, Boursiac Y, Luu D-T, Santoni V, Shahzad Z, Verdoucq L. Aquaporins in plants. Physiol Rev 2015;95(4):1321–58.
[6] Deshmukh RK, Sonah H, Bélanger RR. Plant Aquaporins: genome-wide identification, transcriptomics, proteomics, and advanced analytical tools. Front Plant Sci 2016;7:1896.
[7] Pommerrenig B, Diehn TA, Bienert GP. Metalloido-porins: Essentiality of Nodulin 26-like intrinsic proteins in metalloid transport. Plant Sci 2015;238:212–27.
[8] Jahn TP, Bienert GP. MIPs and their roles in the exchange of metalloids. Springer Science & Business Media; 2011.
[9] Saitoh Y, Mitani-Ueno N, Saito K, Matsuki K, Huang S, Yang L, et al. Structural basis for high selectivity of a rice silicon channel Lsi1. Nat Commun 2021;12(1):1–14.
[10] van den Berg B, Pedebos C, Bolla JR, Robinson CV, Basle A, Khalid S. Structural basis for silicic acid uptake by higher plants. J Mol Biol 2021;433(21):167226.
[11] Ma JF, Yamaji N, Mitani N, Xu X-Y, Su Y-H, McGrath SP, Zhao F-J. Transporters of arsenite in rice and their role in arsenic accumulation in rice grain. Proc Nat Acad Sci 2008;105(29):9931–5.
[12] Mitani N, Yamaji N, Ma JF. Characterization of substrate specificity of a rice silicon transporter, Lsi1. Pflügers Archiv-Eur J Physiol 2008;456(4):679–86.
[13] Vats S, Sudhakaran S, Bhardwaj A, Mandlik R, Sharma Y, Kumar S, et al. Targeting aquaporins to alleviate hazardous metal (loid) s imposed stress in plants. J Hazard Mater 2021;408:124910.
[14] van den Berg B, Pedebos C, Bolla JR, Robinson CV, Baslé A, Khalid S. Structural basis for silicic acid uptake by higher plants. J Mol Biol 2021;433(21):167226.
[15] Jensen MØ, Tajkhorshid E, Schulten K. Electrostatic tuning of permeation and selectivity in aquaporin water channels. Biophys J 2003;85(5):2884–99.
[16] Sabir F, Di Pizio A, Loureiro-Dias MC, Casini A, Soveral G, Prista C. Insights into the selectivity mechanisms of grapevine NIP aquaporins. Int J Mol Sci 2020;21(18):6697.
[17] Mitani-Ueno N, Yamaji N, Zhao F-J, Ma JF. The aromatic/arginine selectivity filter of NIP aquaporins plays a critical role in substrate selectivity for silicon, boron, and arsenic. J Exp Bot 2011;62(12):4391–8.
[18] Eswar N, Eramian D, Webb B, Shen M-Y, Sali A. Protein structure modeling with MODELLER. In: Structural proteomics. Springer; 2008. p. 145–59.
[19] Frisch MJ. Gaussian09, http://www.gaussian.com, 2009.
[20] Jo S, Kim T, Iyer VG, Im W. CHARMM-GUI: a web-based graphical user interface for CHARMM. J Comput Chem 2008;29(11):1859–65.
[21] Lee J, Cheng X, Swails JM, Yeom MS, Eastman PK, Lemkul JA, et al. CHARMM-GUI input generator for NAMD, GROMACS, AMBER, OpenMM, and CHARMM/OpenMM simulations using the CHARMM36 additive force field. J Chem Theory Comput 2016;12(1):405–13.
[22] Van Der Spoel D, Lindahl E, Hess B, Groenhof G, Mark AE, Berendsen HJ. GROMACS: fast, flexible, and free. J Comput Chem 2005;26(16):1701–18.
[23] Wang D, Weng J, Wang W. Glycerol transport through the aquaglyceroporin GlpF: bridging dynamics and kinetics with atomic simulation. Chem Sci 2019;10(29):6957–65.
[24] Smart OS, Neduvelil JG, Wang X, Wallace B, Sansom MS. HOLE: a program for the analysis of the pore dimensions of ion channel structural models. J Mol Graph 1996;14(6):354–60.
[25] Humphrey W, Dalke A, Schulten K. VMD: visual molecular dynamics. J Mol Graph 1996;14(1):33–8.
[26] Deshmukh R, Sonah H, Belanger RR. New evidence defining the evolutionary path of aquaporins regulating silicon uptake in land plants. J Exp Bot 2020;71(21):6775–88.
[27] Verkman A. Aquaporins. Curr Biol 2013;23(2):R52–5.
[28] Wang Y, Schulten K, Tajkhorshid E. What makes an aquaporin a glycerol channel? A comparative study of AqpZ and GlpF. Structure 2005;13(8):1107–18.
[29] Hub JS, De Groot BL. Mechanism of selectivity in aquaporins and aquaglyceroporins. Proc Nat Acad Sci 2008;105(4):1198–203.

[30] Zerbetto De Palma G, Armentia L, Vitali V, Zeida A, Estrin D, Alleva K. Gating in plant plasma membrane aquaporins: the involvement of leucine in the formation of a pore constriction in the closed state. FEBS J 2019;286 (17):3473–87.
[31] Azad AK, Yoshikawa N, Ishikawa T, Sawa Y, Shibata H. Substitution of a single amino acid residue in the aromatic/arginine selectivity filter alters the transport profiles of tonoplast aquaporin homologs. Biochim Biophys Acta (BBA)-Biomembr 2012;1818(1):1–11.
[32] Wang Y, Xiao E, Wu G, Bai Q, Xu F, Ji X, et al. The roles of selectivity filters in determining aluminum transport by AtNIP1; 2. Plant Signal Behav 2021;16 (12):1991686.
[33] Horner A, Zocher F, Preiner J, Ollinger N, Siligan C, Akimov SA, et al. The mobility of single-file water molecules is governed by the number of H-bonds they may form with channel-lining residues. Sci Adv 2015;1(2):e1400083.
[34] de Groot BL, Engel A, Grubmüller H. A refined structure of human aquaporin-1. FEBS Lett 2001;504(3):206–11.
[35] Tajkhorshid E, Nollert P, Jensen MØ, Miercke LJ, O'Connell J, Stroud RM, et al. Control of the selectivity of the aquaporin water channel family by global orientational tuning. Science 2002;296(5567):525–30.
[36] Deshmukh R, Bélanger RR. Molecular evolution of aquaporins and silicon influx in plants. Funct Ecol 2016;30(8):1277–85.
[37] Liu Q, Wang H, Zhang Z, Wu J, Feng Y, Zhu Z. Divergence in function and expression of the NOD26-like intrinsic proteins in plants. BMC Genom 2009;10 (1):1–13.
[38] Liu Q, Zhu Z. Functional divergence of the NIP III subgroup proteins involved altered selective constraints and positive selection. BMC Plant Biol 2010;10 (1):1–12.
[39] Li T, Choi W-G, Wallace IS, Baudry J, Roberts DM. Arabidopsis thaliana NIP7; 1: an anther-specific boric acid transporter of the aquaporin superfamily regulated by an unusual tyrosine in helix 2 of the transport pore. Biochemistry 2011;50(31):6633–41.
[40] Törnroth-Horsefield S, Hedfalk K, Fischer G, Lindkvist-Petersson K, Neutze R. Structural insights into eukaryotic aquaporin regulation. FEBS Lett 2010;584 (12):2580–8.
[41] Kourghi M, Pei JV, De Ieso ML, Flynn G, Yool AJ. Bumetanide derivatives AqB007 and AqB011 selectively block the aquaporin-1 ion channel conductance and slow cancer cell migration. Mol Pharmacol 2016;89 (1):133–40.
[42] Kourghi M, De Ieso ML, Nourmohammadi S, Pei JV, Yool AJ. Identification of loop D domain amino acids in the human Aquaporin-1 channel involved in activation of the ionic conductance and inhibition by AqB011. Front Chem 2018;6:142.
[43] Kitchen P, Conner MT, Bill RM, Conner AC. Structural determinants of oligomerization of the aquaporin-4 channel. J Biol Chem 2016;291 (13):6858–71.
[44] Deshmukh RK, Vivancos J, Ramakrishnan G, Guérin V, Carpentier G, Sonah H, et al. A precise spacing between the NPA domains of aquaporins is essential for silicon permeability in plants. Plant J 2015;83(3):489–500.
[45] Frick A, Järvå M, Törnroth-Horsefield S. Structural basis for pH gating of plant aquaporins. FEBS Lett 2013;587(7):989–93.
[46] Calvanese L, D'Auria G, Vangone A, Falcigno L, Oliva R. Structural basis for mutations of human aquaporins associated to genetic diseases. Int J Mol Sci 2018;19(6):1577.
[47] Dingwell DA, Brown LS, Ladizhansky V. Structure of the functionally important extracellular loop C of human aquaporin 1 obtained by solid-state NMR under nearly physiological conditions. J Phys Chem B 2019;123(36):7700–10.
[48] Wang S, Ing C, Emami S, Jiang Y, Liang H, Pomès RG, Brown LS, Ladizhansky V. Structure and dynamics of extracellular loops in human Aquaporin-1 from solid-state NMR and molecular dynamics. J Phys Chem B 2016;120 (37):9887–902.
[49] Ping Z, Zhou F, Lin X, Su H. Coupled mutations-enabled glycerol transportation in an aquaporin Z mutant. ACS Omega 2018;3(4):4113–22.
[50] Zhang H, Verkman A. Evidence against involvement of aquaporin-4 in cell–cell adhesion. J Mol Biol 2008;382(5):1136–43.
[51] Kumari S, Taginik G, Varadaraj S, Varadaraj K. Positively charged amino acid residues in the extracellular loops A and C of lens aquaporin 0 interact with the negative charges in the plasma membrane to facilitate cell-to-cell adhesion. Exp Eye Res 2019;185:107682.
[52] Xie H, Ma S, Zhao Y, Zhou H, Tong Q, Chen Y, et al. Molecular mechanisms of mercury-sensitive aquaporins. J Am Chem Soc 2022;144(48):22229–41.
[53] Francisca R-C, Alejandra M-L-M, Bárbara A, Herrera R. PIPs from Fragaria vesca: A structural analysis of native and mutated protein. J Mol Graph Model 2022;117:108310.
[54] Whiteman SA, Nühse TS, Ashford DA, Sanders D, Maathuis FJ. A proteomic and phosphoproteomic analysis of Oryza sativa plasma membrane and vacuolar membrane. Plant J 2008;56(1):146–56.
[55] Li Z, Umar Khan M, Yan X, Mu D, Xie Y, Waqas M, et al. Deciphering the molecular mechanisms of chilling tolerance in Lsi1-overexpressing rice. Int J Mol Sci 2022;23(9):4667.
[56] Saitoh Y, Suga M. Structure and function of a silicic acid channel Lsi1. Front Plant Sci 2022:3441.